**Particulate matter (PM) episodes at a suburban site in Hong Kong: evolution of PM characteristics and role of photochemistry in secondary aerosol formation**

Yi Ming Qin[1], Yong Jie Li[2,*], Hao Wang[3], Berto Paul Yok Long Lee[3], Dan Dan Huang[1], and Chak Keung Chan[1,3,4,*]

[1]Department of Chemical and Biomolecular Engineering, Hong Kong University of Science and Technology, Hong Kong, China

[2]Faculty of Science and Technology, University of Macau, Taipa, Macau, China

[3]Division of Environment, Hong Kong University of Science and Technology, Hong Kong, China

[4]School of Energy and Environment, City University of Hong Kong, Hong Kong, China


[*]To Whom Correspondence Should be Addressed

Chak K. Chan: AC1-G5716, School of Energy and Environment, City University of Hong Kong,

Tat Chee Avenue, Kowloon, Hong Kong, China

Tel: (852) 3442-5593; Fax: (852) 3442-0688

Email: chak.k.chan@cityu.edu.hk

Yong Jie Li: E11-3017, Faculty of Science and Technology, University of Macau, E11, Avenida da Universidade,

Taipa, Macau, China

Tel: (853) 8822-4943; Fax: (853) 8822-2426

Email: yongjieli@umac.mo

1    **Abstract**

2    Episodes with high concentrations of particulate matter (PM) across the seasons were investigated during four

3    one-month campaigns at a suburban site in Hong Kong. High-resolution time-of-flight aerosol mass spectrometer

4    (HR-ToF-AMS) measurements revealed that both regional transport and secondary formation contributed to high

5    PM levels during the episodes at this site. Based on distinct meteorological conditions, episodes were categorized

6    into three types: liquid water content (LWC), solar irradiance (IR), and long-range transport (LRT). Despite the

7    difference in meteorological conditions, all episodes were characterized by a high fraction of sulfate (45%-56%) and

8    organics (23%-34%). However, aerosols in LWC episodes were less aged, consisting of the lowest fraction of

9    secondary organics aerosols (SOA) and the highest fraction of small particles. Large particles mixed internally while

10   freshly formed small particles mixed externally in LWC episodes. Aerosols in LRT episodes, by contrast, were the

11   most aged and consisted of the highest proportion of low-volatility oxygenated organic aerosols (LVOOA) and the

12   lowest proportion of small particles. Both small and large particles mixed externally in LRT episodes. The highest

13   proportion of semi-volatile oxygenated organic aerosols (SVOOA) and a medium proportion of small particles were

14   observed in IR episodes. Both small and large particles were likely externally mixed during IR episodes. Unlike in

15   the other two types of episodes, in IR episodes aerosols experienced the most dramatic size increase and diurnal

16   variation, with a time lag between SVOOA and LVOOA and a gradual increase in carbon oxidation state ($\overline{OS}_c \approx$

17   $2 \times O:C-H:C$). Five out of ten episodes were of the IR type, further reflecting the importance of this type of episode.

18   The evolution of aerosol components in one particular episode of the IR type, which exhibited a clear land-sea

19   breeze pattern, was examined in detail. Sulfate and SOA due to photochemical aging were very efficiently produced

20   during the course of six hours. The "less-oxidized" SOA (SVOOA) was initially formed at a higher rate than the

21   "more-oxidized" SOA (LVOOA). The SVOOA transformed to LVOOA at the later stage of photochemical aging.

22   This transformation was further supported by mass spectral analysis, which showed an increase in the most oxidized

23   ion ($CO_2^+$) and decreases in moderately oxidized ones ($C_2H_3O^+$, $C_3H_3O^+$ and $C_3H_5O^+$). By measuring the physical

24   and chemical properties of PM in a highly time-resolved manner, the current study was able to demonstrate the

25   dynamic and complex nature of PM transformation during high-PM episodes.

## 1. Introduction

Hong Kong and the rest of the Pearl River Delta (PRD) in China have been battling air pollution episodes as a result of rapid economic development and urbanization in the region (Ho et al., 2003; Zhong et al., 2013). Meteorological conditions may govern the regional and long-range transport of air pollutants to Hong Kong. For example, northerly winds can bring pollutants from the inland areas to Hong Kong, and have been suggested to be responsible for regional air pollution events in winter (Fang et al., 1999; Huang et al., 2009, 2014b). The majority of earlier studies used filter sampling with a low time resolution of hours to days, and so were unable to track the temporal chemical transformation in high particulate matter (PM) episodes. This limitation has hindered our understanding of the dynamic nature of PM undergoing rapid chemical transformations. Such chemical transformation can occur within short time periods (e.g., within a day), and so do other physicochemical properties such as hygroscopic and optical properties. High-time-resolution chemical characterization techniques, for example the Aerodyne high-resolution time-of-flight aerosol mass spectrometer (HR-ToF-AMS), offer a temporal resolution of a few minutes. These techniques can thus provide valuable information on rapid changes in the PM composition, facilitating more detailed analysis of pollution events (Decarlo et al., 2006). HR-ToF-AMS measurements also give the size distributions of components (DeCarlo et al., 2008; Lee et al., 2013b). These data can reveal the origin, formation and atmospheric processing mechanisms of PM (Seinfeld and Pandis, 2006; Shiraiwa et al., 2013), but they remain under-utilized in most aerosol mass spectrometer (AMS) studies.

Secondary formation has been recognized as an important route leading to high PM concentrations worldwide (Zhang et al., 2015a) and is the main culprit for haze episodes in cities across China (Huang et al., 2014a). Secondary organic aerosol (SOA) has been shown to dominate over primary organic aerosol (POA) after a few hours of photochemical aging, for instance, in Mexico City (Decarlo et al., 2010; Volkamer et al., 2006), Pasadena (Hayes et al., 2013) and Tokyo (Takegawa et al., 2006). Semi-volatile oxygenated organic aerosol (SVOOA), which serves as a proxy for less-oxidized SOA, has been shown to transform to low-volatility oxygenated organic aerosol (LVOOA), which serves as a proxy for more-oxidized SOA, in laboratory experiments (Alfarra et al., 2012; Jimenez et al., 2009). Such transformation process may contribute substantially to the accumulation of PM, leading to episodic events that are frequently observed in the fast-developing city clusters in China (Huang et al., 2012; Zhang et al., 2015b).

53        We conducted four one-month campaigns in each of the four seasons at the Hong Kong University of Science

54    and Technology (HKUST) Air Quality Research Supersite (AQRS) from May 2011 to February 2012 using an

55    Aerodyne HR-ToF-AMS for non-refractory $PM_1$ (PM with aerodynamic diameter less than 1 micron). In our

56    previous studies, we found that photochemical oxidation during a haze episode and aqueous-phase reactions during

57    two foggy periods both led to a high degree of oxygenation of organics due to aging in gas phase and/or aqueous

58    phase with substantial SOA formation (Lee et al., 2013 and Li et al., 2013). In spring and summer, SOA, with

59    abundant SVOOA, was more likely to form locally. The oxygen-to-carbon atomic ratio (O:C) and average carbon

60    oxidation state ($\overline{OS}_c$) peaked in the afternoon in spring and summer (Li et al., 2015). In autumn and winter, LVOOA

61    dominated in SOA. The O:C ratio and $\overline{OS}_c$ showed little diurnal variation. Huang et al. (2015) estimated the

62    contents of organic sulfur compounds in Hong Kong in September 2011. They highlighted the importance of both

63    aqueous-phase processing and regional influence for the formation of organic sulfur compounds. Closure analysis

64    was performed between the PM hygroscopicity measured by a hygroscopic tandem differential mobility analyzer

65    (HTDMA) and chemical composition measured by an HR-ToF-AMS and a constant growth factor of 1.18 for

66    organics was found to be adequate for a good closure, given the dominant contribution of the very hygroscopic

67    sulfate at this suburban site (Cheung et al., 2016; Yeung et al., 2014). Meng et al. ( 2014) found that the aerosol

68    hygroscopic parameter (*k*) decreased with an increasing organic-to-inorganic volume ratio. Furthermore, the

69    concentration of cloud condensation nuclei (CCN) was found to be more sensitive to the mixing state and

70    hygroscopicity of the particles at a high supersaturation (SS)=0.70% and a low SS=0.15%, respectively.

71        The above studies primarily focused on the analysis of campaign-average scenarios, without specifically

72    looking at episodic events that occurred during the campaign.  In the current study, we investigated the chemical

73    transformation and size evolution of secondary aerosols in high particulate matter episodes across the four seasons.

74    Specifically, we examined in detail the photochemical evolution in a particular episode in which local influences

75    were dominant. Results from the current study reveal the rapid evolution of secondary aerosols and are relevant to

76    other megacities with large precursor input and high photochemical activity.

77    **2.    Experimental Section**

78    **2.1.  Sampling Site and Measurements**

79        The sampling periods were from 25 April to 1 June 2011 (spring), from 1 September to 29 September 2011

80    (summer), from 28 October to 15 December 2011 (autumn), and from 19 January to 1 March 2012 (winter). HR-

81   ToF-AMS measurements were conducted at the HKUST AQRS (22°20'N, 114°16'E). The HKUST supersite is

82   located on the campus of HKUST, which sits on the hillside of Clear Water Bay on the east coast of Hong Kong that

83   has relatively low population density. There is little local emission around the site. Two minor local sources include

84   Clear Water Bay Road and a small student canteen.  The Clear Water Bay Road is located outside of the campus and

85   has mild traffic. The student canteen within 200m of the site, which operates only from 18:00LT (local time) until

86   midnight. The HR-ToF-AMS operating procedure, data analysis and species determination have been discussed in

87   Lee et al. (2013a), Li et al. (2015) and Huang et al. (2015). Briefly, the AMS was operated alternatively between the

88   V+PToF combined mode and the W-mode for 5 min each. A collection efficiency of 0.5 was employed for

89   measurements at this site, where the particles have overwhelmingly dominant sulfate content (Aiken et al., 2009; Li

90   et al., 2013). Concentrations of methanesulfonic acid (MSA) and organosulfates (OS) were estimated by combining

91   the V-mode data for total concentrations and the W-mode data for high-resolution mass spectral analysis for specific

92   ions (Huang et al., 2015). Mass spectra of organic sulfur compounds were obtained from standards in laboratory

93   experiments to support the W-mode data analysis (Huang et al., 2015). We further calculated the particle liquid

94   water content (LWC) by applying E-AIM II (Clegg et al., 1998) to explore the effects of aqueous processing on $PM_1$

95   composition. Gaseous species (CO, $CO_2$, $SO_2$, NO, $NO_2$, and $O_3$) were measured with standard gas analyzers

96   (Teledyne API). Volatile organic compounds (VOCs) were measured by gas chromatography (Synspec GC955).

97   Meteorological parameters were measured by an automatic weather station mounted on a tower right next to the

98   supersite. Particle hygroscopicity and size distribution measurements have previously been taken with a HR-ToF-

99   AMS at this site (Cheung et al., 2015; Man et al., 2015; Meng et al., 2014; Yeung et al., 2014), and direct reference

100  to the resulting publications will be made where necessary.

101  **2.2.   Data analysis**

102  **2.2.1.   Criteria for an episodic event**

103  The total non-refractory $PM_1$ (NR-$PM_1$) concentration showed little seasonal variation, with monthly averages

104  ranging from 14.3 to 15.9 μg m$^{-3}$ as reported by Li et al. (2015). In this work, we defined episodic events according

105  to the following criteria: 1) lasting for at least 24 hours; 2) daily NR-$PM_1$ average mass concentration exceeding 15

106  μg m$^{-3}$ (overall monthly averaged concentration); and 3) maximum concentration exceeding 30 μg m$^{-3}$. According to

107  these criteria, 10 episodic events were identified in the campaigns as shown in Figure S1.

108  **2.2.2.   Source apportionment**

109    Following the results in Li et al. (2015), 72-hour backward air trajectory analysis and positive matrix

110    factorization (PMF) analysis were performed. Briefly, the back trajectory analysis was run at an elevation of 300 m

111    using the HYSPLIT-4.8 (Hybrid Single-Particle Lagrangian Integrated Trajectory) model developed by

112    NOAA/ARL (U.S. National Oceanic and Air Administration/Air Resources Laboratory). We classified air masses

113    affecting Hong Kong into long-, medium-, and short-range transport patterns for transport distances of 1000 km,

114    between 500 and 1000 km, and less than 500 km, respectively (Su et al., 2015).

115    For PMF analysis, a four-factor solution with hydrocarbon-like organic aerosols (HOA), cooking organic

116    aerosols (COA), SVOOA, and LVOOA was adopted as in Li et al. (2015). During episodic events, HOA and COA

117    contributed insignificantly (less than 6% and 5% respectively) to total organic aerosol (OA). Since we are interested

118    in SOA transformation, HOA and COA were combined into one POA factor in the following discussion.

119    **2.2.3.    Size distribution**

120    Size distributions of aerosol species are obtained with the HR-ToF-AMS when a set of pre-selected m/z is

121    scanned as a function of the particle time of flight. We focus on the size distribution analysis of sulfate and organics

122    because of their overwhelming dominance in NR-PM$_1$. The raw 10-min mass-size distributions of organics and

123    sulfate during the episodic events were averaged over various time periods pertaining to the resolution (e.g. 24 hours,

124    1 hour). The average size distributions were then fitted by the peak fitting tool Multipeak Fit V2 provided by Igor

125    Pro (Wavemetrics) using two log-normal peaks. The peaks were chosen such that the fit residuals were minimized.

126    The two fitted peaks of the size distributions will hereafter be referred to as the small particle mode and the large

127    particle mode. Fitting examples can be found in Figure S2. We will focus on the most important fitting parameters:

128    the particle mass-mode diameter (vacuum aerodynamic diameter, $D_{va}$) indicating the shift in particle size and the

129    integrated peak areas of the small particle mode and the large particle mode indicating the changes in mass

130    concentrations of larger or smaller particles.

131    **2.2.4.    Photochemical age**

132    The photochemical age is useful for studying the extent of photochemical processing in an air mass. One way to

133    estimate the photochemical age ($\Delta t$) is by the ratio of a less reactive hydrocarbon to a more reactive one (Kleinman,

134    2003):

$$\Delta t= \frac{Ln(\frac{C_j}{C_i}*\frac{C_{i0}}{C_{j0}})}{(k_i-k_j)[OH]} \qquad (1)$$

135

136   in which $C_i$ and $C_j$ are concentrations of hydrocarbons $i$ and $j$ at time $t$, whereas $C_{i0}$ and $C_{j0}$ are concentrations of

137   hydrocarbons $i$ and $j$ at time 0. The symbols $k_i$ and $k_j$ are their respective rates of reaction with hydroxyl radicals

138   (OH). Hofzumahaus et al. (2009) reported a high average OH concentration of $15 \times 10^6$ molecules cm$^{-3}$ around noon

139   in the PRD region, much higher than model predictions. Zhou et al. (2014) used an OH concentration of $5.2 \times 10^6$

140   molecules cm$^{-3}$ in their calulation of photochamical age in the PRD region.  Lacking definitive estimates, we used a

141   conservative OH concentration of $1.5 \times 10^6$ molecule cm$^{-3}$ (Hayes et al., 2013; Mao et al., 2009) for the discussion of

142   oxidation trends in this study. The ratio of benzene to toluene has been widely used (El Haddad et al., 2013) because

143   of their similar emission sources and significantly different rates of reaction with OH radicals ($k_{benzene-OH}= 1.23 \times 10^{-12}$

144   $^{12}$ cm$^3$ molecule$^{-1}$ s$^{-1}$; $k_{toluene-OH}= 6.0 \times 10^{-12}$ cm$^3$ molecule$^{-1}$ s$^{-1}$ at 298K) (Atkinson Roger, 2000). Because toluene

145   reacts more rapidly with OH radicals than does benzene, it is depleted more quickly, resulting in higher

146   benzene/toluene ratios in aged air masses. However, the photochemical age can deviate when fresh pollutants are

147   added to an aged air mass. Since fresh pollutants were insignificant after 10:00 (i.e. no significant peaks of benzene

148   and toluene after 10:00; see Figure S3), we set the start time at 10:00 for the discussion of photochemical aging.

149   **3.   Results and Discussion**

150   **3.1. Meteorological conditions and classification of episodes**

151       Table 1 summarizes the meteorological conditions, PM$_1$ concentrations, and the estimated LWC in the 10 high

152   PM episodes. All of the episodes involved air masses that originated over East Asia from the north, northeast or

153   northwest of Hong Kong, and swept over part of the PRD region before reaching the site. Seven of the 10 episodes

154   (E1-E7) were characterized by medium-range trajectories and the other three (E8-E10) by long-range trajectories.

155   The individual trajectories are shown in Figure S4. E1 and E2 had much lower solar irradiance (IR) but higher LWC

156   than the other episodes, which distinguished them from the other medium-range transport episodes. Thus, E1 and E2

157   were categorized as episodes of the LWC type (medium-range transport with high LWC and low IR) and the other

158   medium-range transport episodes as episodes of the IR type (medium-range transport with high IR and low LWC).

159   Li et al. (2013) referred to E1 and E2 as foggy episodes, while Li et al. (2013) and Lee et al. (2013a) referred to E3

160    as a hazy episode. The long-range transport episodes might be less associated with the local site-specific conditions

161    and were categorized as episodes of the LRT type.

162    High concentrations of PM can have a number of causes, including enhanced primary emissions (Ji et al., 2014),

163    concentrating effects due to a decrease in the height of the planetary boundary layer (Petäjä et al., 2016), regional

164    transport (Huang et al., 2009), as well as active secondary formation (Hayes et al., 2013). Local primary emissions

165    were not very significant at this site, as can be seen from the low contribution of POA (less than 6%) throughout the

166    whole campaign. As an indicator for primary PM, elemental carbon (EC) concentrations in $PM_{2.5}$ filter sampling at

167    this site from March 2011 to February 2012 were also found to be low throughout the year (0.86 ± 0.53

168    µg/m$^3$)(Huang et al., 2014b). Boundary layer dynamics on the high PM days can be a factor affecting PM

169    concentration, but the effects were likely minimal as the highest concentration was usually observed during the day

170    at higher mixing heights (Figure S5). Therefore, regional transport and active secondary formation would be the

171    most probable causes for the episodic events of high PM concentrations at this suburban site. More detailed

172    meteorological conditions with chemical characteristics in each episode can be found in Figure S5.

173    As is apparent from Table 1, the occurrence of different types of episodes exhibits a seasonal trend. LWC

174    episodes occurred only in spring and LRT episodes only in winter, while IR episodes took place in spring, summer

175    and autumn. This result is consistent with previous results (Huang et al., 2009) in that the frequency of high PM

176    days in Hong Kong had a strong seasonal variation. In winter, the overwhelming northerly wind brings pollutants

177    via long-range transport (Fang et al., 1999). In spring, foggy days with high PM levels are common due to the

178    moisture-laden air masses coming in from the sea and aqueous-phase processing of particulate species (Li et al.,

179    2013). In summer and autumn, however, hazy days are mainly due to high photochemical activities in this

180    subtropical area, resulting in the formation of secondary aerosols (Hu et al., 2008; Zhou et al., 2014).

181    **3.2. Chemical characteristics of high PM episodes**

182    Figure 1 shows the chemical constituents of NR-PM$_1$ in the three types of episodes. It is apparent that sulfate

183    dominated in all types of episodes. In Hong Kong, sulfate is largely regarded as a major regional pollutant with little

184    spatial variability, as in the rest of the PRD (Hagler et al., 2006; LOUIE et al., 2005). Nitrate contributed less than 4%

185    in LWC episodes and IR episodes, but more than 7% in LRT episodes.  As LRT episodes occurred in wintertime,

186    the higher nitrate concentration was likely driven by gas-particle partitioning of ammonium nitrate to the particle at

187 low temperatures (Seinfeld and Pandis, 2006). Using the PMF-resolved SVOOA and LVOOA as proxies for less-

188 oxidized and more-oxidized SOA respectively (Zhang et al., 2011), more details of OA can be revealed. SVOOA

189 had higher contributions in IR episodes, while LVOOA contributed roughly twice as much as SVOOA did in LRT

190 episodes, because the air mass was already quite aged when reached the site. LVOOA and SVOOA made similar

191 contributions in LWC episodes.

192     Figure 2 shows the diurnal variations of the NR-PM$_1$ species, PMF-resolved organic factors, as well as O$_x$

193 (O$_3$+NO$_2$) in these three types of episodes. SVOOA and LVOOA as well as O$_x$ increased during the day in IR

194 episodes, with a time lag between SVOOA and LVOOA. A similar time lag was also observed between SVOOA

195 and LVOOA in the Yangtze River Delta (YRD), another fast developing region of China (Huang et al., 2012). These

196 delays may be the result of conversions from SVOOA to LVOOA in the afternoon. We explore such a possibility in

197 Section 3.6. SVOOA and LVOOA both exhibit flat diurnal patterns in LWC episodes and LRT episodes.

198     Elemental analysis of OA (ratios of H:C, O:C, N:C, S:C and OM:OC) from the high resolution mass spectra

199 provides useful information to assess OA evolution. Recently, Canagaratna et al. (2015) used an updated (Improved-

200 Ambient) method to estimate O:C and H:C ratios, and reported 27% higher O:C ratios and 11% higher H:C ratios

201 than those estimated using the original (Aiken-Ambient) method. Recalculating the elemental ratios for the

202 September dataset using the updated method shows little difference from those obtained by simply applying the

203 respective factors of 1.27 and 1.11 to the O:C and H:C ratios (Figure S6). Hence, the O:C and H:C ratios in this

204 study were corrected by factors of 1.27 and 1.11, respectively, with Aiken-Ambient values reported in our previous

205 studies. In the Van Krevelen diagram (Heald et al., 2010; Ng et al., 2011) shown in Figure 3a, data points for LWC

206 episodes (blue) fall into a lower O:C region than do the data points for IR (red) and LRT episodes (green).

207 Although aqueous-phase processing might generate highly oxygenated organic compounds (Li et al.,

208 2016; Mazzoleni et al., 2010; Zhao et al., 2013), sampling by the AMS was only limited to interstitial

209 particles and a portion of very small fog droplets after drying. This can also lead to O:C ratios lower than

210 those in IR periods when most of the photochemically oxidized OA were effectively sampled. Even though

211 data points for IR episodes and LRT episodes have similar slopes and intercepts in the Van Krevelen diagram, data

212 points for IR episodes had a much wider spread. These trends are also reflected in the diurnal patterns of carbon

213 oxidation state ($\overline{OS}_c \approx 2\times$O:C-H:C) (Kroll et al., 2011) in Figure 3b. The $\overline{OS}_c$ diurnal pattern in LRT episodes was

214 relatively flat, suggesting that oxidized organics were mostly transported to the site with minor in-situ oxidation.

215     The $\overline{OS_c}$ in IR episodes gradually increased from 09:00 until 15:00. Similar trends were observed for $O_x$, LVOOA

216     and to a less extent, SVOOA. With all these combined, we believe that the local photochemical processing of OA

217     was more likely at play in IR episodes than the long-range transport of processed aerosols.

218

219     **3.3. Size distributions of sulfate and organics**

220     Figure 4 shows the peak fitting results of the type-averaged size distributions of organics and sulfate mass. The

221     mass-mode diameters ($D_{va}$) for both the small and large modes of organics and sulfate did not differ considerably

222     across the episode types (differing by less than 5%). Within each type of episode, sulfate had a smaller fraction of

223     small particle mode than organics did, indicating that sulfate was relatively aged while organics received

224     contributions from local fresh emissions. LWC episodes received the largest contribution from small mode sulfate

225     because of some local influences whereas LRT episodes received the smallest contribution with relatively little local

226     activities. The oxidation mechanisms, however, might be different. Aqueous phase oxidation may dominate in

227     LWC episodes while photochemical oxidation may dominate in IR episodes.

228     Various studies have analyzed the particle mixing state using single-particle instruments such as the aerosol time-

229     of-flight mass spectrometer (Healy et al., 2013, 2014; Yang et al., 2012) and the single-particle aerosol mass

230     spectrometer (Wang et al., 2015). Particle mixing state can also be inferred from particle size information obtained

231     with the AMS. If the organics and sulfate are internally mixed (i.e. they exist in the same particle), their diameters

232     should be strongly correlated with each other and their size should grow at a similar rate. The observed strong

233     correlation and slope of unity (correlated in time and size) suggest that these species are likely internally mixed,

234     although we cannot completely exclude the possibility of external mixing. On the other hand, if the mode diameters

235     of sulfate and organics did not change coherently and exhibit a strong correlation with a slope close to unity, these

236     particles were more likely externally mixed. Bahreini et al. (2003) have used such correlations in size to indicate the

237     mixing states of species. In our study, the large mode diameters of organics and sulfate were strongly correlated

238     (Pearson's R value equals 0.7) with a slope close to unity in LWC episodes (Figure 5), suggesting that organics and

239     sulfate were likely internally mixed in the large particles. However, these conditions of correlation and slope are

240     necessary but not sufficient evidence for internal mixing. This internal mixing may occur during the process of local

241     aqueous oxidation. In IR episodes, during which local photochemical oxidation may have a more obvious influence,

242    larger particles do not mix well internally (poor correlation between the large mode diameters of organics and

243    sulfate with Rpr = 0.2). As discussed in Section 3.2, in IR episodes, organics showed a clear noontime peak

244    associated with local photochemical activities while sulfate was still mainly a regional pollutant. As a result, large

245    particles of organics and sulfates were very likely to have been externally mixed during IR episodes. A good

246    correlation (Rpr = 0.7) with the slope deviating substantially from unity (slope = 0.5) was observed in LRT episodes.

247    As long-range transport was the dominant process causing high PM levels during LRT episodes, organics and

248    sulfate would have been brought to the site together, so their large mode diameters tend to be strongly correlated.

249    However, they may have different origins and may also have undergone different aging processes during the course

250    of long-range transport, and thus their mode diameters would be different. The correlations between the small mode

251    diameters of organics and sulfate were notably weaker, with Rpr=0.5 in LWC episodes, Rpr=0.2 in IR episodes, and

252    Rpr=0.2 in LRT episodes, suggesting that freshly formed small particles mixed externally.

253    As discussed earlier, there may be some local atmospheric processing of aerosols in LWC and IR episodes but not

254    in LRT episodes. Therefore, we further explored the mechanisms underlying the atmospheric processing of LWC

255    and IR episodes based on the size variations before and during episodic events. Figure 6 shows the particle mass

256    mode diameters and areas (concentrations) in the LWC and IR types of episodes. We obtained the percentage

257    changes in mode diameters by comparing the smallest diameter before the episode and the largest diameter during

258    the episode for each episode. These percentages in each episode was then averaged to obtain the percentage changes

259    for each episode type. The results show that the changes in mode diameter were small in the LWC episodes: -2.5%

260    for small mode organics, +8.1% for large mode organics, +1.6% for small mode sulfate, and -3% for large mode

261    sulfate. In contrast, the changes in mode diameters changes were much more drastic in the IR episodes: +51.3% for

262    small mode organics, +40.5% for large mode organics, +45.4% for small mode sulfate, and +35.9% for large mode

263    sulfate. Furthermore, particle size usually increased more rapidly before the IR episodes (shaded in blue in Figure 6)

264    than during the episodes (shaded in orange). With fewer pre-existing particles before the episodes, particle growth

265    likely via condensation and reactive uptake of semi-volatile components was more rapid than during the episodes.

266    The number concentration is discussed in detail in SI.

267    **3.4. Local photochemical formation and evolution of PM: A case study**

268    **3.4.1.    Time series of species during the local photochemical episode**

269    Because of the high frequency of occurrence of IR episodes, we chose one IR episode (E4) to examine the

270    evolution of the aerosols with photochemical oxidation. This particular episode (E4) was under the influence of a

271    clear land-sea breeze pattern with weak winds (Figure 7), a typical meteorological phenomenon that affects air

272    pollution dynamics at this coastal city (Lee et al., 2013a). As can be seen from Figure 7, the maximum wind speed

273    was less than 2 m s$^{-1}$ while the average wind speed was approximately 0.5 m s$^{-1}$. The wind direction changed from

274    northerly to easterly between 06:00 and 10:00 and remained easterly until 20:00, when it changed clockwise from

275    easterly back to northerly. Under such conditions, local photochemical activities can lead to effective production and

276    accumulation of air pollutants. Time series of organics, sulfate, ammonium, nitrate, MSA, OS, PMF-resolved

277    organic factors, some gaseous species, as well as meteorological parameters were analyzed. Most NR-PM$_1$ species

278    showed clear diurnal variations. Figure 7 shows that organics increased from a roughly constant concentration of 10

279    µg m$^{-3}$ at night until 09:00 to its highest concentration of 16.6 µg m$^{-3}$ at 13:00, while sulfate showed a mild increase

280    at 06:00 and then a sharp increase at 10:30 to reach its highest concentration of 17.4 µg m$^{-3}$ at 16:00. They were

281    overall consistent with the increasing trend of irradiance, an indicator of photochemical activities, in the afternoon.

282    Nitrate concentration was high (2.5 µg m$^{-3}$) in the morning and started to decrease from 12:30 onwards to reach 0.3

283    µg m$^{-3}$ by 16:00, likely attributable to vertical dilution due to a rise in the height of the planetary boundary layer, or

284    alternatively evaporation of ammonium nitrate at higher temperatures and lower RH values (Seinfeld and Pandis,

285    2006). Wind direction started to change at 20:00, when all the NR-PM$_1$ species were at their lowest concentrations.

286    POA concentration increased from 2.5 µg m$^{-3}$ at 00:00 to about 5 µg m$^{-3}$ at 06:00, which might be due to the

287    lowering of the planetary boundary layer. Conversely, expansion of the boundary layer early in the morning could

288    help disperse the POA. The increase in LVOOA lagged behind that in SVOOA. Starting from 06:00, SVOOA

289    concentration increased rapidly and peaked at approximately 13:00, coinciding with the IR peak, possibly due to

290    SOA formation. LVOOA gradually increased from 12:00 and peaked at 14:00, similar to sulfate. The time lag

291    suggests that some conversion from less-oxidized to more-oxidized SOA might have occurred in the afternoon.

292    Evaporation at the elevated temperature of 30ºC throughout the afternoon might also have led to the decrease in

293    SVOOA, as with nitrate. The diurnal variation of MSA shows a noontime peak, consistent with the trend of

294    irradiance. In contrast, OS did not show a clear noontime peak, since OS at this site were likely affected by inland

295    transportation (Huang et al., 2015).

296    **3.4.2.    Changes in size distribution**

297    As shown Figure 8, before 06:00, the size distributions of sulfate and organics were both dominated by a mass

298    mode diameter of 500 to 600 nm. During 06:00-09:00, a shoulder at 200 nm appeared in the size distribution of

299    sulfate and in that of organics, indicating some fresh sulfate and organics were formed or emitted (possibly POA).

300    As photochemical reactions proceeded (09:00-18:00), the shoulder of $D_{va}$ at 200 nm became weaker and the size

301    distributions shifted to the larger end. It should be noted that during the whole aging process, the size distributions of

302    organics were broader than those of sulfate since organics were a mixture of numerous constituents from different

303    primary sources and reaction products formed via different atmospheric processes. The shifts in size distribution

304    suggest that secondary aerosol particles with sulfate and organics aged gradually and grew into larger particles.

305    **3.4.3.    Photochemical production of secondary species**

306    We examine the daytime photochemical activity during E4 by looking at the $SO_2$ oxidation and changes in the

307    degree of oxygenation of particulate organics. The sulfur oxidation ratio (SOR) has been used to evaluate the extent

308    of atmospheric oxidation of $SO_2$ to sulfate (Squizzato et al., 2013; Wang et al., 2005). Figure 9c shows the increase

309    in SOR from 0.2 at 9:00 to 0.7 at 18:00, indicating an efficient conversion from $SO_2$ to sulfate during daytime in this

310    episode. Figure 9b shows that the $\overline{OS_c}$ increased sharply near 11:00. $\overline{OS_c}$ was high after 18:00 because most of the

311    organics in PM had been converted to highly oxidized organic compounds during the aging process. Indeed, during

312    this period, LVOOA was the dominant OA component (Figure 7). The increases in SOR and $\overline{OS_c}$ coincided with

313    the increase in the ratio of benzene to toluene (Figure 9). The oxidation of sulfur species and organic species reflects

314    efficient oxidation during this photochemical episode.

315    To semi-quantitatively evaluate the efficiency of SOA and sulfate formation, the changes in SOA/$\Delta$CO,

316    MSA/$\Delta$CO, and sulfate/$\Delta$CO are plotted in Figure 10 as a function of photochemical age from 10:00 to 18:00. $\Delta$CO,

317    defined as the measured CO concentration minus the minimum CO concentration (see Figure 7 for the time series of

318    CO), is assumed to be a conservative tracer of urban combustion emissions. The perturbations of CO concentration

319    by photochemical formation from VOC or destruction by OH radicals were thought to be negligible over such a

320    short timescale (less than eight hours) (Griffin et al., 2007). Normalization of species concentrations to the $\Delta$CO

321    concentration is expected to reduce the effect of dilution (Hayes et al., 2013; Zhou et al., 2014).

322    From 10:00 to 18:00, sulfate/$\Delta$CO increased by a factor of 7-8 as photochemical activity increased on a

323    timescale of approximately 6 h, with a formation rate (indicated by the slope of species/$\Delta$CO vs. photochemical age)

324    of approximlately 48 $\mu$g m$^{-3}$ ppm$^{-1}$ h$^{-1}$. MSA/$\Delta$CO also increased by a factor of approximately 3 at a rate of 0.05 $\mu$g

325    $m^{-3}$ $ppm^{-1}$ $h^{-1}$ during photochemical aging. The good correlation of MSA production with the photochemical age

326    suggests that MSA originated from the reaction of gaseous dimethyl sulfide with OH radicals (Barnes et al., 2006).

327    For comparison, Bardouki et al. (2003) also found that MSA and OH radicals covaried over the northeastern coast of

328    Crete. As shown in Figure 10c, SOA/$\Delta$CO increased by approximately a factor of 2 with the slope of 7.2 $\mu g$ $m^{-3}$

329    $ppm^{-1}$ $h^{-1}$ (8.07 $\mu g$ $sm^{-3}$ $ppm^{-1}$ $h^{-1}$). A shallower slope (approximately 4.0 to 4.5 $\mu g$ $sm^{-3}$ $ppm^{-1}$ $h^{-1}$) was observed in

330    Pasadena, California from May to June (Hayes et al., 2013) while a similar slope (6.18 $\mu g$ $m^{-3}$ $ppm^{-1}$ $h^{-1}$) was

331    observed in a previous study in Hong Kong in August (Zhou et al., 2014). This indicates that the SOA production in

332    Hong Kong during the local in situ photochemical oxidation in summer is high.

333      More interestingly, SVOOA/$\Delta$CO increased during the first three hours but decreased slightly after 13:00, even

334    as photochemical age increased. In contrast, LVOOA/$\Delta$CO increased steadily throughout the whole stage. After

335    photochemical processing for 6 h, LVOOA/$\Delta$CO increased by approximately a factor of 20, from 2.3 $\mu g$ $m^{-3}$ $ppm^{-1}$

336    to 49.4 $\mu g$ $m^{-3}$ $ppm^{-1}$. Even though both SVOOA/$\Delta$CO and LVOOA/$\Delta$CO increased in the first stage, they did so at

337    slightly different rates, where SVOOA/$\Delta$CO increased faster than LVOOA/$\Delta$CO. This suggests that the production

338    of SVOOA was more efficient than that of LVOOA in the first stage. However, in the later stage of SOA formation,

339    the net productions of SVOOA were negative, which indicates that SVOOA may have photchemically converted to

340    LVOOA. As discussed earlier, the input of POA and VOC was limited to the early morning in our study. SVOOA

341    was consumed more quickly to form LVOOA than was replenished through further production in the late afternoon.

342    The situation where limited precursors exist to replenish fresh SOA (even under strong photochemical activity)

343    might also occur in other non-urban atmospheric environments, and thus may have an implication for OA

344    transformation in general.

345    ### 3.4.4. Mass spectral evolution

346      Figure 11a shows the evolving organic mass spectra during E4 (corresponding to the period of photochemical

347    aging). Eight spectra at one-hour intervals from 10:00 to 18:00 are shown from top to bottom. Two changes in the

348    mass spectra with photochemical processes were apparent: 1) decreases in the signal intensities of relatively high

349    m/z ions (e.g., m/z 55, 57,67, 69, etc.), which indicates greater fragmentation (C-C bond cleavage) with

350    photochemical oxidation; and 2) increases in the mass concentrations of ions having m/z values of 28 (mainly $CO^+$)

351    and 44 (mainly $CO_2^+$), which presumably come from aldehyde, ketone and carboxylic acid (Ng et al., 2011). These

352    changes are also reflected in the relative intensity changes of hydrocarbon-like and oxygen-containing ions such as

353     $C_4H_7^+$, $C_2H_3O^+$ and $CO_2^+$ (Figure 11b, c). The fractions of tracers of primary organic aerosols $C_3H_7^+$(m/z 43), $C_4H_7^+$

354     (m/z 55) and $C_4H_9^+$ (m/z 57) (Lambe et al., 2012) decreased. On the other hand, ion fractions of $C_2H_3O^+$ (m/z 43),

355     $C_3H_3O^+$ (m/z 55) and $C_3H_5O^+$ (m/z 57) increased until 13:00 (corresponding to the peak of SVOOA), followed by

356     the decrease of these moderately oxygenated ions. These ions are predominantly from non-acid oxygenates, and are

357     usually associated with less-oxidized SOA. However, The most oxidized ions, $CO_2^+$ (m/z 44), which is thought to be

358     the marker of more-oxidized SOA, increased continuously. As a result, the mass spectra, which were initially

359     SVOOA-like, evolved to become LVOOA-like with increasing photochemical age (Figure 11d). Overall, this

360     spectral analysis indicates increasingly oxidized organics, as long carbon chains became more functionalized and

361     fragmented after extensive oxidation (Alfarra et al., 2012; Kroll et al., 2009). Such an observation implies efficient

362     transformation of OA within a few hours of photochemical aging, a timescale that could be relevant to chemical

363     transport models concerning SOA formation.

364       **4. Conclusion**

365     High-resolution HR-ToF-AMS measurements were taken during four one-month campaigns in suburban Hong

366     Kong to illustrate the evolution of high PM episodic events across the seasons. Three types of episodes, medium-

367     range transport with high particle liquid water content (LWC episodes), medium-range transport with high solar

368     irradiance (IR episodes), and long-range transport (LRT episodes), were captured based on synoptic meteorological

369     conditions. Which type of episode occurred depended on the season, with LWC episodes occurring only in spring

370     and LRT episodes only in winter, while IR episodes took place throughout the year except in winter. Sulfate was the

371     major constituent of NR-PM$_1$ during all episodic events. The contribution of secondary organic species, including

372     SVOOA and LVOOA, varied across episode types, with more SVOOA in the IR episodes and more LVOOA in the

373     LRT episodes. Unlike in the other two types of episodes, in IR episodes organics experienced the most dramatic

374     diurnal variation, with a time lag between SVOOA and LVOOA. This variation was associated with Ox, indicating

375     the conversions from less-oxidized to more-oxidized SOA under photochemical oxidation. Elemental analysis

376     involving the Van Krevelen diagram and carbon oxidation state ($\overline{OS}_c \approx 2 \times$O:C-H:C) further showed that organics in

377     IR were gradually oxidized.

378     Fitted mass-mode diameters for both the small and the large mode of organics remained roughly constant across

379     episode types, while sulfate had a constant small mode diameter in all three types of episodes but a slightly

380     increased large mode diameter in IR episodes. The fraction of small particles decreased from LWC episodes to IR

381 episodes then to LRT episodes, suggesting that aerosols from long-range transport were more aged and dominated

382 by large particles while episodes under a greater influence of local processes had a higher proportion of fresher

383 small particles. Large particles mixed internally only in LWC episodes, and were more likely to mix externally in IR

384 and LRT episodes. Freshly formed small particles mixed externally in all types of episodes. In IR episodes, aerosols

385 underwent an obvious size increase, while in LWC episodes, the size increase was much less drastic.

386     Because of the high frequency of IR episodes, we picked one particular IR episode featuring land-sea breeze to

387 examine in detail the evolution of aerosol components. Photochemical aging led to mode size shifting for sulfate and

388 organics, indicating particle growth. Increases in the sulfur oxidation ratio and carbon oxidation state were also

389 observed as the aerosols became more aged, which indicates that secondary inorganic species sulfate and SOA were

390 very efficiently produced within six hours of photochemical aging. In the earlier stage of aging, "less-oxidizd"

391 SOA—SVOOA—was formed at a higher rate than "more-oxidized" SOA—LVOOA. SVOOA clearly transformed

392 to LVOOA at the later stage of photochemical aging, resulting in a 20-fold increase in LVOOA. This conversion

393 was further supported by mass spectral analysis, which showed an increase in the most oxidized ion ($CO_2^+$) and

394 decreases in moderately oxidized ones ($C_2H_3O^+$, $C_3H_3O^+$ and $C_3H_5O^+$). With real-time size-resolved chemical

395 composition data, we demonstrated that aerosol components can transform very efficiently in just a few hours, a

396 process that is essential in understanding the dynamic nature of aerosol evolution during episodes with high PM

397 concentrations.

404

405

406

407

408

409

410

**References**

Aiken, A. C., Salcedo, D., Cubison, M. J., Huffman, J. A., DeCarlo, P. F., Ulbrich, I. M., Docherty, K. S., Sueper, D., Kimmel, J. R., Worsnop, D. R., Trimborn, A., Northway, M., Stone, E. A., Schauer, J. J., Volkamer, R. M., Fortner, E., de Foy, B., Wang, J., Laskin, A., Shutthanandan, V., Zheng, J., Zhang, R., Gaffney, J., Marley, N. A., Paredes-Miranda, G., Arnott, W. P., Molina, L. T., Sosa, G. and Jimenez, J. L.: Mexico City aerosol analysis during MILAGRO using high resolution aerosol mass spectrometry at the urban supersite (T0) – Part 1: Fine particle composition and organic source apportionment, Atmos. Chem. Phys., 9(17), 6633–6653, doi:10.5194/acp-9-6633-2009, 2009.

Alfarra, M. R., Hamilton, J. F., Wyche, K. P., Good, N., Ward, M. W., Carr, T., Barley, M. H., Monks, P. S., Jenkin, M. E., Lewis, A. C. and McFiggans, G. B.: The effect of photochemical ageing and initial precursor concentration on the composition and hygroscopic properties of β-caryophyllene secondary organic aerosol, Atmos. Chem. Phys., 12(14), 6417–6436, doi:10.5194/acp-12-6417-2012, 2012.

Atkinson Roger, J. A.: Atmospheric degradation of volatile methyl-silicon compounds, Environ. Sci. Technol., 34(10), 1970–1976, doi:10.1021/es9910053, 2000.

Bardouki, H., Berresheim, H., Vrekoussis, M., Sciare, J., Kouvarakis, G., Oikonomou, K., Schneider, J. and Mihalopoulos, N.: Gaseous (DMS, MSA, $SO_2$, $H_2SO_4$ and DMSO) and particulate (sulfate and methanesulfonate) sulfur species over the northeastern coast of Crete, Atmos. Chem. Phys., 3(5), 1871–1886, doi:10.5194/acp-3-1871-2003, 2003.

Barnes, I., Hjorth, J. and Mihalapoulos, N.: Dimethyl sulfide and dimethyl sulfoxide and their oxidation in the atmosphere, Chem. Rev., 106(3), 940–975, doi:10.1021/cr020529+, 2006.

Canagaratna, M. R., Jimenez, J. L., Kroll, J. H., Chen, Q., Kessler, S. H., Massoli, P., Hildebrandt Ruiz, L., Fortner, E., Williams, L. R., Wilson, K. R., Surratt, J. D., Donahue, N. M., Jayne, J. T. and Worsnop, D. R.: Elemental ratio measurements of organic compounds using aerosol mass spectrometry: characterization, improved calibration, and implications, Atmos. Chem. Phys., 15(1), 253–272, doi:10.5194/acp-15-253-2015, 2015.

Cheung, H. H. Y., Yeung, M. C., Li, Y. J., Lee, B. P. and Chan, C. K.: Relative Humidity-Dependent HTDMA Measurements of Ambient Aerosols at the HKUST Supersite in Hong Kong, China, Aerosol Sci. Technol., 49(8), 643–654, doi:10.1080/02786826.2015.1058482, 2015.

Cheung, H. H. Y., Tan, H., Xu, H., Li, F., Wu, C., Yu, J. Z. and Chan, C. K.: Measurements of non-volatile aerosols with a VTDMA and their correlations with carbonaceous aerosols in Guangzhou, China, Atmos. Chem. Phys., 16(13), 8431–8446, doi:10.5194/acp-16-8431-2016, 2016.

Clegg, S. L., Brimblecombe, P. and Wexler, A. S.: Thermodynamic Model of the System $H^+ - NH_4^+ - Na^+ - SO_4^{2-} - NO_3^- - Cl^- - H_2O$ at 298.15 K, J. Phys. Chem. A, 102(12), 2155–2171, doi:10.1021/jp973043j, 1998.

Decarlo, P. F., Kimmel, J. R., Trimborn, A., Northway, M. J., Jayne, J. T., Aiken, A. C., Gonin, M., Fuhrer, K., Horvath, T., Docherty, K. S., Worsnop, D. R. and Jimenez, J. L.: Field-Deployable, High-Resolution, Time-of-Flight Aerosol Mass Spectrometer, Anal. Chem., 78(24), 8281–8289, doi:8410.1029/2001JD001213.Analytical, 2006.

DeCarlo, P. F., Dunlea, E. J., Kimmel, J. R., Aiken, a. C., Sueper, D., Crounse, J., Wennberg, P. O., Emmons, L., Shinozuka, Y., Clarke, a., Zhou, J., Tomlinson, J., Collins, D. R., Knapp, D., Weinheimer, A. J., Montzka, D. D., Campos, T. and Jimenez, J. L.: Fast airborne aerosol size and chemistry measurements above Mexico City and Central Mexico during the MILAGRO campaign, Atmos. Chem. Phys., 8(14), 4027–4048, doi:10.5194/acp-8-4027-2008, 2008.

Decarlo, P. F., Ulbrich, I. M., Crounse, J., De Foy, B., Dunlea, E. J., Aiken, a. C., Knapp, D., Weinheimer, A. J.,

453 Campos, T., Wennberg, P. O. and Jimenez, J. L.: Investigation of the sources and processing of organic aerosol over
454 the Central Mexican Plateau from aircraft measurements during MILAGRO, Atmos. Chem. Phys., 10(12), 5257–
455 5280, doi:10.5194/acp-10-5257-2010, 2010.

456 Fang, M., Zheng, M., Wang, F., Chim, K. and Kot, S.: The long-range transport of aerosols from northern China to
457 Hong Kong - a multi-technique study, Atmos. Environ., 33(11), 1803–1817 [online] Available from:
458 http://repository.ust.hk/ir/Record/1783.1-28286 (Accessed 9 November 2015), 1999.

459 Griffin, R. J., Chen, J., Carmody, K., Vutukuru, S. and Dabdub, D.: Contribution of gas phase oxidation of volatile
460 organic compounds to atmospheric carbon monoxide levels in two areas of the United States, J. Geophys. Res.,
461 112(D10), D10S17, doi:10.1029/2006JD007602, 2007.

462 El Haddad, I., D'Anna, B., Temime-Roussel, B., Nicolas, M., Boreave, a., Favez, O., Voisin, D., Sciare, J., George,
463 C., Jaffrezo, J.-L., Wortham, H. and Marchand, N.: Towards a better understanding of the origins, chemical
464 composition and aging of oxygenated organic aerosols: case study of a Mediterranean industrialized environment,
465 Marseille, Atmos. Chem. Phys., 13(15), 7875–7894, doi:10.5194/acp-13-7875-2013, 2013.

466 Hagler, G. S. W., Bergin, M. H., Salmon, L. G., Yu, J. Z., Wan, E. C. H., Zheng, M., Zeng, L. M., Kiang, C. S.,
467 Zhang, Y. H., Lau, A. K. H. and Schauer, J. J.: Source areas and chemical composition of fine particulate matter in
468 the Pearl River Delta region of China, Atmos. Environ., 40(20), 3802–3815, doi:10.1016/j.atmosenv.2006.02.032,
469 2006.

470 Hayes, P. L., Ortega, a. M., Cubison, M. J., Froyd, K. D., Zhao, Y., Cliff, S. S., Hu, W. W., Toohey, D. W., Flynn, J.
471 H., Lefer, B. L., Grossberg, N., Alvarez, S., Rappenglück, B., Taylor, J. W., Allan, J. D., Holloway, J. S., Gilman, J.
472 B., Kuster, W. C., De Gouw, J. a., Massoli, P., Zhang, X., Liu, J., Weber, R. J., Corrigan, a. L., Russell, L. M.,
473 Isaacman, G., Worton, D. R., Kreisberg, N. M., Goldstein, a. H., Thalman, R., Waxman, E. M., Volkamer, R., Lin,
474 Y. H., Surratt, J. D., Kleindienst, T. E., Offenberg, J. H., Dusanter, S., Griffith, S., Stevens, P. S., Brioude, J.,
475 Angevine, W. M. and Jimenez, J. L.: Organic aerosol composition and sources in Pasadena, California, during the
476 2010 CalNex campaign, J. Geophys. Res. Atmos., 118(16), 9233–9257, doi:10.1002/jgrd.50530, 2013.

477 Heald, C. L., Kroll, J. H., Jimenez, J. L., Docherty, K. S., Decarlo, P. F., Aiken, a. C., Chen, Q., Martin, S. T.,
478 Farmer, D. K. and Artaxo, P.: A simplified description of the evolution of organic aerosol composition in the
479 atmosphere, Geophys. Res. Lett., 37(8), doi:10.1029/2010GL042737, 2010.

480 Ho, K. ., Lee, S. ., Chan, C. K., Yu, J. C., Chow, J. C. and Yao, X. .: Characterization of chemical species in PM2.5
481 and PM10 aerosols in Hong Kong, Atmos. Environ., 37(1), 31–39, doi:10.1016/S1352-2310(02)00804-X, 2003.

482 Hofzumahaus, A., Rohrer, F., Lu, K., Bohn, B., Brauers, T., Chang, C.-C., Fuchs, H., Holland, F., Kita, K., Kondo,
483 Y., Li, X., Lou, S., Shao, M., Zeng, L., Wahner, A. and Zhang, Y.: Amplified trace gas removal in the troposphere.,
484 Science, 324(5935), 1702–1704, doi:10.1126/science.1164566, 2009.

485 Hu, D., Bian, Q., Li, T. W. Y., Lau, A. K. H. and Yu, J. Z.: Contributions of isoprene, monoterpenes, β-
486 caryophyllene, and toluene to secondary organic aerosols in Hong Kong during the summer of 2006, J. Geophys.
487 Res. Atmos., 113(22), 1–14, doi:10.1029/2008JD010437, 2008.

488 Huang, D. D., Li, Y. J., Lee, B. P. and Chan, C. K.: Analysis of Organic Sulfur Compounds in Atmospheric
489 Aerosols at the HKUST Supersite in Hong Kong Using HR-ToF-AMS, Environ. Sci. Technol., 150305134049007,
490 doi:10.1021/es5056269, 2015.

491 Huang, R.-J., Zhang, Y., Bozzetti, C., Ho, K.-F., Cao, J.-J., Han, Y., Daellenbach, K. R., Slowik, J. G., Platt, S. M.,
492 Canonaco, F., Zotter, P., Wolf, R., Pieber, S. M., Bruns, E. a., Crippa, M., Ciarelli, G., Piazzalunga, A.,
493 Schwikowski, M., Abbaszade, G., Schnelle-Kreis, J., Zimmermann, R., An, Z., Szidat, S., Baltensperger, U.,
494 Haddad, I. El and Prévôt, A. S. H.: High secondary aerosol contribution to particulate pollution during haze events
495 in China, Nature, doi:10.1038/nature13774, 2014a.

496 Huang, X.-F. F., Yu, J. Z., Yuan, Z. B., Lau, A. K. H. H. and Louie, P. K. K. K.: Source analysis of high particulate
497 matter days in Hong Kong, Atmos. Environ., 43(6), 1196–1203, doi:10.1016/j.atmosenv.2008.10.013, 2009.

498 Huang, X. F., He, L. Y., Xue, L., Sun, T. L., Zeng, L. W., Gong, Z. H., Hu, M. and Zhu, T.: Highly time-resolved
499 chemical characterization of atmospheric fine particles during 2010 Shanghai World Expo, Atmos. Chem. Phys.,
500 12(11), 4897–4907, doi:10.5194/acp-12-4897-2012, 2012.

501  Huang, X. H. H., Bian, Q., Ng, W. M., Louie, P. K. K. and Yu, J. Z.: Characterization of PM2.5 major components
502  and source investigation in suburban Hong Kong: A one year monitoring study, Aerosol Air Qual. Res., 14(1), 237–
503  250, doi:10.4209/aaqr.2013.01.0020, 2014b.

504  Ji, D., Li, L., Wang, Y., Zhang, J., Cheng, M., Sun, Y., Liu, Z., Wang, L., Tang, G., Hu, B., Chao, N., Wen, T. and
505  Miao, H.: The heaviest particulate air-pollution episodes occurred in northern China in January, 2013: Insights
506  gained from observation, Atmos. Environ., 92, 546–556, doi:10.1016/j.atmosenv.2014.04.048, 2014.

507  Jimenez, J. L., Canagaratna, M. R., Donahue, N. M., Prevot,  a S. H., Zhang, Q., Kroll, J. H., DeCarlo, P. F., Allan, J.
508  D., Coe, H., Ng, N. L., Aiken,  a C., Docherty, K. S., Ulbrich, I. M., Grieshop,  a P., Robinson,  a L., Duplissy, J.,
509  Smith, J. D., Wilson, K. R., Lanz, V. a, Hueglin, C., Sun, Y. L., Tian, J., Laaksonen,  a, Raatikainen, T., Rautiainen,
510  J., Vaattovaara, P., Ehn, M., Kulmala, M., Tomlinson, J. M., Collins, D. R., Cubison, M. J., Dunlea, E. J., Huffman,
511  J. a, Onasch, T. B., Alfarra, M. R., Williams, P. I., Bower, K., Kondo, Y., Schneider, J., Drewnick, F., Borrmann, S.,
512  Weimer, S., Demerjian, K., Salcedo, D., Cottrell, L., Griffin, R., Takami,  a, Miyoshi, T., Hatakeyama, S., Shimono,
513  a, Sun, J. Y., Zhang, Y. M., Dzepina, K., Kimmel, J. R., Sueper, D., Jayne, J. T., Herndon, S. C., Trimborn,  a M.,
514  Williams, L. R., Wood, E. C., Middlebrook,  a M., Kolb, C. E., Baltensperger, U. and Worsnop, D. R.: Evolution of
515  organic aerosols in the atmosphere., Science, 326(5959), 1525–1529, doi:10.1126/science.1180353, 2009.

516  Kleinman, L. I.: Photochemical age determinations in the Phoenix metropolitan area, J. Geophys. Res., 108(D3), 1–
517  14, doi:10.1029/2002JD002621, 2003.

518  Kroll, J. H., Smith, J. D., Che, D. L., Kessler, S. H., Worsnop, D. R. and Wilson, K. R.: Measurement of
519  fragmentation and functionalization pathways in the heterogeneous oxidation of oxidized organic aerosol., Phys.
520  Chem. Chem. Phys., 11(36), 8005–14, doi:10.1039/b905289e, 2009.

521  Kroll, J. H., Donahue, N. M., Jimenez, J. L., Kessler, S. H., Canagaratna, M. R., Wilson, K. R., Altieri, K. E.,
522  Mazzoleni, L. R., Wozniak, A. S., Bluhm, H., Mysak, E. R., Smith, J. D., Kolb, C. E. and Worsnop, D. R.: Carbon
523  oxidation state as a metric for describing the chemistry of atmospheric organic aerosol, Nat. Chem., 3(2), 133–139,
524  doi:10.1038/nchem.948, 2011.

525  Lambe, A. T., Onasch, T. B., Croasdale, D. R., Wright, J. P., Martin, A. T., Franklin, J. P., Massoli, P., Kroll, J. H.,
526  Canagaratna, M. R., Brune, W. H., Worsnop, D. R. and Davidovits, P.: Transitions from Functionalization to
527  Fragmentation Reactions of Laboratory Secondary Organic Aerosol (SOA) Generated from the OH Oxidation of
528  Alkane Precursors, Environ. Sci. Technol., 46(10), 5430–5437, doi:Doi 10.1021/Es300274t, 2012.

529  Lee, B. P., Li, Y. J., Yu, J. Z., Louie, P. K. K. and Chan, C. K.: Physical and chemical characterization of ambient
530  aerosol by HR-ToF-AMS at a suburban site in Hong Kong during springtime 2011, J. Geophys. Res. Atmos.,
531  118(15), 8625–8639, doi:10.1002/jgrd.50658, 2013a.

532  Lee, B. P., Li, Y. J., Flagan, R. C., Lo, C. and Chan, C. K.: Sizing Characterization of the Fast-Mobility Particle
533  Sizer (FMPS) Against SMPS and HR-ToF-AMS, Aerosol Sci. Technol., 47(9), 1030–1037,
534  doi:10.1080/02786826.2013.810809, 2013b.

535  Li, Y., Pöschl, U. and Shiraiwa, M.: Molecular corridors and parameterizations of volatility in the chemical
536  evolution of organic aerosols, Atmos. Chem. Phys., 16(5), 3327–3344, doi:10.5194/acp-16-3327-2016, 2016.

537  Li, Y. J., Lee, B. Y. L., Yu, J. Z., Ng, N. L. and Chan, C. K.: Evaluating the degree of oxygenation of organic
538  aerosol during foggy and hazy days in Hong Kong using high-resolution time-of-flight aerosol mass spectrometry
539  (HR-ToF-AMS), Atmos. Chem. Phys., 13(17), 8739–8753, doi:10.5194/acp-13-8739-2013, 2013.

540  Li, Y. J., Lee, B. P., Su, L., Fung, J. C. H. and Chan, C. K.: Seasonal characteristics of fine particulate matter (PM)
541  based on high-resolution time-of-flight aerosol mass spectrometric (HR-ToF-AMS) measurements at the HKUST
542  Supersite in Hong Kong, Atmos. Chem. Phys., 15(1), 37–53, doi:10.5194/acp-15-37-2015, 2015.

543  LOUIE, P., WATSON, J., CHOW, J., CHEN, A., SIN, D. and LAU, A.: Seasonal characteristics and regional
544  transport of PM in Hong Kong, Atmos. Environ., 39(9), 1695–1710, doi:10.1016/j.atmosenv.2004.11.017, 2005.

545  Man, H., Zhu, Y., Ji, F., Yao, X., Lau, N. T., Li, Y., Lee, B. P. and Chan, C. K.: Comparison of daytime and
546  nighttime new particle growth at the HKUST supersite in Hong Kong., Environ. Sci. Technol., 49(12), 7170–8,
547  doi:10.1021/acs.est.5b02143, 2015.

548 Mao, J., Ren, X., Brune, W. H., Olson, J. R., Crawford, J. H., Fried, A., Huey, L. G., Cohen, R. C., Heikes, B.,
549 Singh, H. B., Blake, D. R., Sachse, G. W., Diskin, G. S., Hall, S. R. and Shetter, R. E.: Airborne measurement of
550 OH reactivity during INTEX-B, Atmos. Chem. Phys., 9(1), 163–173, doi:10.5194/acp-9-163-2009, 2009.

551 Mazzoleni, L. R., Ehrmann, B. M., Shen, X., Marshall, A. G. and Collett, J. L.: Water-Soluble Atmospheric Organic
552 Matter in Fog: Exact Masses and Chemical Formula Identification by Ultrahigh-Resolution Fourier Transform Ion
553 Cyclotron Resonance Mass Spectrometry, Environ. Sci. Technol., 44(10), 3690–3697, doi:10.1021/es903409k, 2010.

554 Meng, J. W., Yeung, M. C., Li, Y. J., Lee, B. Y. L. and Chan, C. K.: Size-resolved cloud condensation nuclei (CCN)
555 activity and closure analysis at the HKUST Supersite in Hong Kong, Atmos. Chem. Phys., 14(18), 10267–10282,
556 doi:10.5194/acp-14-10267-2014, 2014.

557 Mohr, C., DeCarlo, P. F., Heringa, M. F., Chirico, R., Slowik, J. G., Richter, R., Reche, C., Alastuey, A., Querol, X.,
558 Seco, R., Pe??uelas, J., Ji???enez, J. L., Crippa, M., Zimmermann, R., Baltensperger, U., Pr??v??ot, A. S. H.,
559 Peñuelas, J., Jiménez, J. L., Crippa, M., Zimmermann, R., Baltensperger, U. and Prévôt, A. S. H.: Identification and
560 quantification of organic aerosol from cooking and other sources in Barcelona using aerosol mass spectrometer data,
561 Atmos. Chem. Phys., 12(4), 1649–1665, doi:10.5194/acp-12-1649-2012, 2012.

562 Ng, N. L., Canagaratna, M. R., Jimenez, J. L., Chhabra, P. S., Seinfeld, J. H. and Worsnop, D. R.: Changes in
563 organic aerosol composition with aging inferred from aerosol mass spectra, Atmos. Chem. Phys., 11(13), 6465–
564 6474, doi:10.5194/acp-11-6465-2011, 2011.

565 Petäjä, T., Järvi, L., Kerminen, V.-M., Ding, A. J., Sun, J. N., Nie, W., Kujansuu, J., Virkkula, A., Yang, X., Fu, C.
566 B., Zilitinkevich, S. and Kulmala, M.: Enhanced air pollution via aerosol-boundary layer feedback in China., Sci.
567 Rep., 6, 18998, doi:10.1038/srep18998, 2016.

568 Seinfeld, J. H. and Pandis, S. N.: ATMOSPHERIC From Air Pollution to Climate Change SECOND EDITION.,
569 2006.

570 Shiraiwa, M., Yee, L. D., Schilling, K. a, Loza, C. L., Craven, J. S., Zuend, A., Ziemann, P. J. and Seinfeld, J. H.:
571 Size distribution dynamics reveal particle-phase chemistry in organic aerosol formation., Proc. Natl. Acad. Sci. U. S.
572 A., 110(29), 11746–50, doi:10.1073/pnas.1307501110, 2013.

573 Squizzato, S., Masiol, M., Brunelli, a., Pistollato, S., Tarabotti, E., Rampazzo, G. and Pavoni, B.: Factors
574 determining the formation of secondary inorganic aerosol: A case study in the Po Valley (Italy), Atmos. Chem.
575 Phys., 13(4), 1927–1939, doi:10.5194/acp-13-1927-2013, 2013.

576 Su, L., Yuan, Z., Fung, J. C. H. and Lau, A. K. H.: A comparison of HYSPLIT backward trajectories generated from
577 two GDAS datasets, Sci. Total Environ., 506–507, 527–537, doi:10.1016/j.scitotenv.2014.11.072, 2015.

578 Takegawa, N., Miyakawa, T., Kondo, Y., Blake, D. R., Kanaya, Y., Koike, M., Fukuda, M., Komazaki, Y.,
579 Miyazaki, Y., Shimono, a. and Takeuchi, T.: Evolution of submicron organic aerosol in polluted air exported from
580 Tokyo, Geophys. Res. Lett., 33(15), 3–7, doi:10.1029/2006GL025815, 2006.

581 Volkamer, R., Jimenez, J. L., San Martini, F., Dzepina, K., Zhang, Q., Salcedo, D., Molina, L. T., Worsnop, D. R.
582 and Molina, M. J.: Secondary organic aerosol formation from anthropogenic air pollution: Rapid and higher than
583 expected, Geophys. Res. Lett., 33(17), L17811, doi:10.1029/2006GL026899, 2006.

584 Wang, Y., Zhuang, G., Tang, A., Yuan, H., Sun, Y., Chen, S. and Zheng, A.: The ion chemistry and the source of
585 PM2.5 aerosol in Beijing, Atmos. Environ., 39(21), 3771–3784, doi:10.1016/j.atmosenv.2005.03.013, 2005.

586 Yeung, M. C., Lee, B. P., Li, Y. J. and Chan, C. K.: Simultaneous HTDMA and HR-ToF-AMS measurements at the
587 HKUST Supersite in Hong Kong in 2011, J. Geophys. Res. Atmos., 119(16), 9864–9883,
588 doi:10.1002/2013JD021146, 2014.

589 Zhang, Q., Jimenez, J. L., Canagaratna, M. R., Ulbrich, I. M., Ng, N. L., Worsnop, D. R. and Sun, Y.:
590 Understanding atmospheric organic aerosols via factor analysis of aerosol mass spectrometry: A review, Anal.
591 Bioanal. Chem., 401(10), 3045–3067, doi:10.1007/s00216-011-5355-y, 2011.

592 Zhang, R., Wang, G., Guo, S., Zamora, M. L., Ying, Q., Lin, Y., Wang, W., Hu, M. and Wang, Y.: Formation of
593 Urban Fine Particulate Matter, Chem. Rev., 115(10), 3803–3855, doi:10.1021/acs.chemrev.5b00067, 2015a.

594 Zhang, Y. W., Zhang, X. Y., Zhang, Y. M., Shen, X. J., Sun, J. Y., Ma, Q. L., Yu, X. M., Zhu, J. L., Zhang, L. and
595 Che, H. C.: Significant concentration changes of chemical components of PM1 in the Yangtze River Delta area of
596 China and the implications for the formation mechanism of heavy haze-fog pollution., Sci. Total Environ., 538, 7–
597 15, doi:10.1016/j.scitotenv.2015.06.104, 2015b.

598 Zhao, Y., Hallar, A. G. and Mazzoleni, L. R.: Atmospheric organic matter in clouds: exact masses and molecular
599 formula identification using ultrahigh-resolution FT-ICR mass spectrometry, Atmos. Chem. Phys., 13(24), 12343–
600 12362, doi:10.5194/acp-13-12343-2013, 2013.

601 Zhong, L., Louie, P. K. K., Zheng, J., Yuan, Z., Yue, D., Ho, J. W. K. and Lau, A. K. H.: Science–policy interplay:
602 Air quality management in the Pearl River Delta region and Hong Kong, Atmos. Environ., 76, 3–10,
603 doi:10.1016/j.atmosenv.2013.03.012, 2013.

604 Zhou, S., Wang, T., Wang, Z., Li, W., Xu, Z., Wang, X., Yuan, C., Poon, C. N., Louie, P. K. K., Luk, C. W. Y. and
605 Wang, W.: Photochemical evolution of organic aerosols observed in urban plumes from Hong Kong and the Pearl
606 River Delta of China, Atmos. Environ., 88, 219–229, doi:10.1016/j.atmosenv.2014.01.032, 2014.

607

**Tables:**

*Table 1 Synopsis of meteorological conditions of high PM episodes*

| Episode | Season | Date | Air mass origin | Wind speed (m s$^{-1}$) | Solar Irradiance (w m$^{-2}$) | Liquid water content (µg m$^{-3}$) | PM$_1$ (µg m$^{-3}$) | PM$_1$ Max (µg m$^{-3}$) | Type |
|---|---|---|---|---|---|---|---|---|---|
| E1 | Spring | 28-30 Apr | M-R[a]/NE[b] | 0.7±0.4 | 41±67 | 47.1±15.9 | 25.5±3.1 | 33.1 | LWC |
| E2 | Spring | 14-16 May | M-R/NE[b] | 1.1±0.8 | 27±61 | 38.6±14.5 | 18.8±6.4 | 32.4 | LWC |
| E3 | Spring | 27-29 May | M-R[a]/NE[b] | 0.9±0.8 | 184±263 | 19.3±9.2 | 28.4±12.6 | 64.1 | IR |
| E4 | Summer | 2 Sep | M-R[a]/NW[b] | 0.5±0.4 | 111±163 | 20.0±3.1 | 22.5±6.1 | 33.7 | IR |
| E5 | Summer | 20-24 Sep | M-R[a]/NE[b] | 2.2±0.5 | 143±234 | 14.9±4.6 | 23.8±4.8 | 35.9 | IR |
| E6 | Autumn | 3 Nov | M-R[a]/NE[b] | 1.3±0.5 | 174±271 | 12.8±5.9 | 15.6±6.2 | 30.0 | IR |
| E7 | Autumn | 13-15 Nov | M-R[a]/NE[b] | 1.2±0.5 | 150±221 | 19.4±7.0 | 23.4±7.0 | 45.2 | IR |
| E8 | Winter | 24-25 Nov | L-R[a]/NE[b] | 1.6±0.5 | 112±174 | 14.1±6.6 | 25.9±6.2 | 38.6 | LRT |
| E9 | Winter | 8 Feb | L-R[a]/N[b] | 2.2±0.6 | 49±74 | 27.8±2.8 | 29.7±8.1 | 41.6 | LRT |
| E10 | Winter | 18-19 Feb | L-R[a]/NE[b] | 1.5±0.6 | 104±170 | 16.0±5.3 | 25.5±9.4 | 64.9 | LRT |

a: Range of air mass orgin: Medium range (M-R); Long range (L-R).
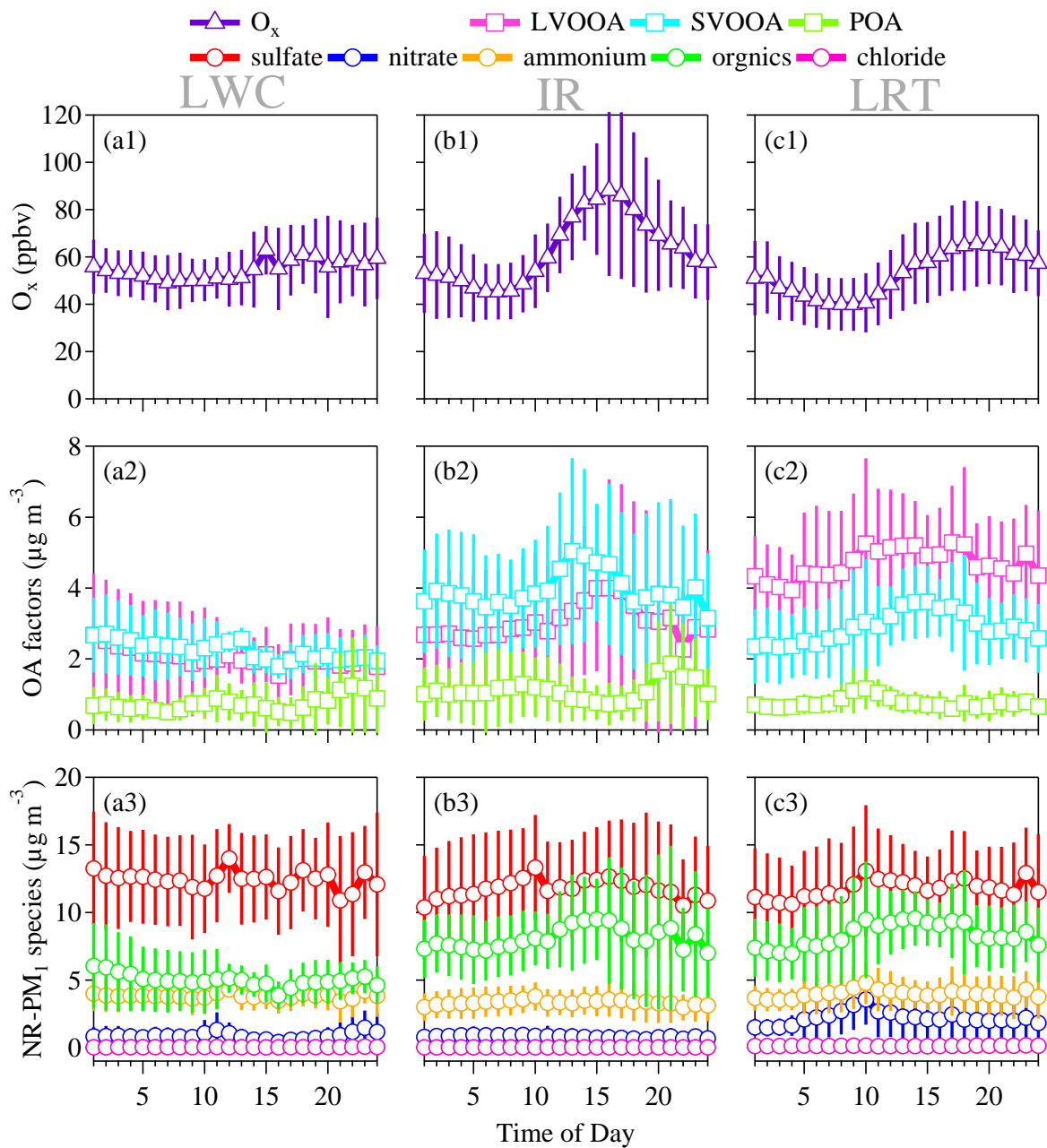b: Direction of air mass origin: Northeast (NE); Northwest(NW); North (N).

**Figures:**

Sulfate Nitrate Ammonium Chloride Organic (POA, SVOOA, LVOOA)
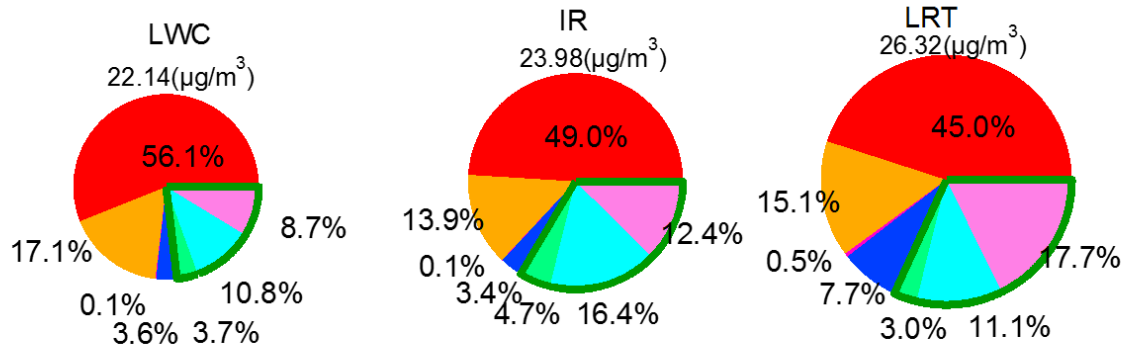


2

3   *Figure 1 Chemical constituents NR-PM$_1$ in LWC, IR and LRT episodes. (LWC: medium-range transport with high*
4   *LWC and low IR; IR: medium-range transport with high IR and low LWC; LRT: long-range transport)*
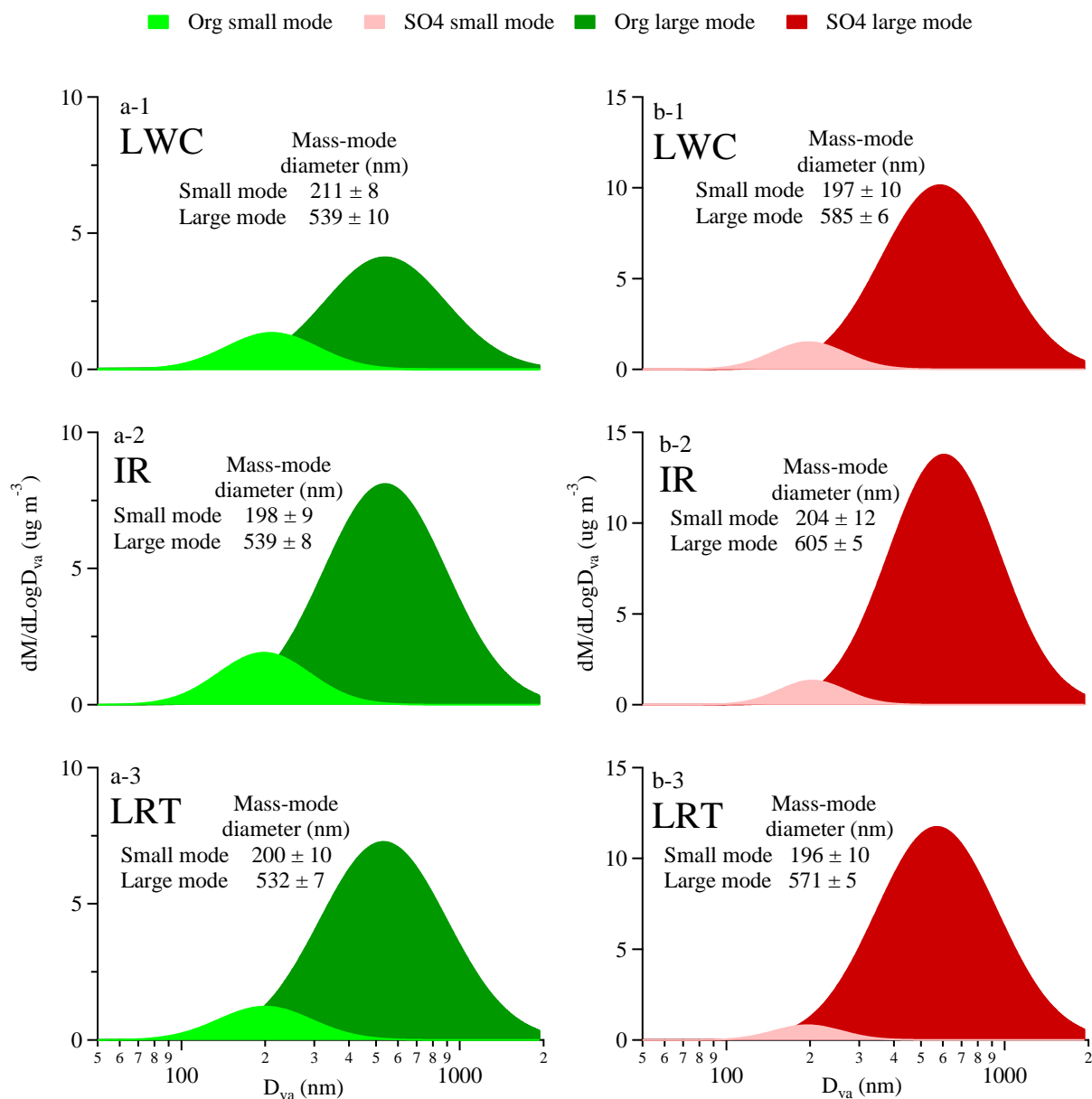
Figure 2 Summary of diurnal variations of the PM$_1$ species, PMF-resolved organics as well as O$_x$ in the three types of episodes. Means are shown as points and standard deviations are as error bars.

8
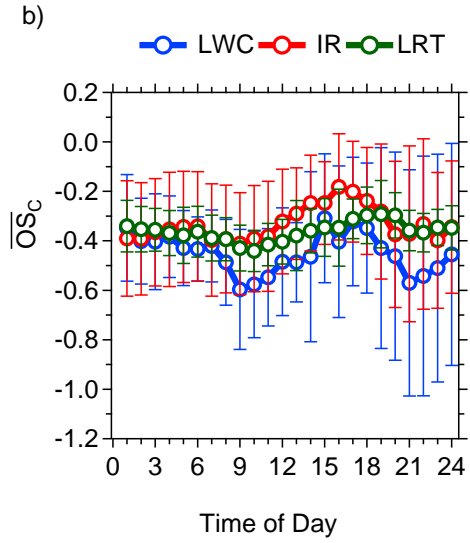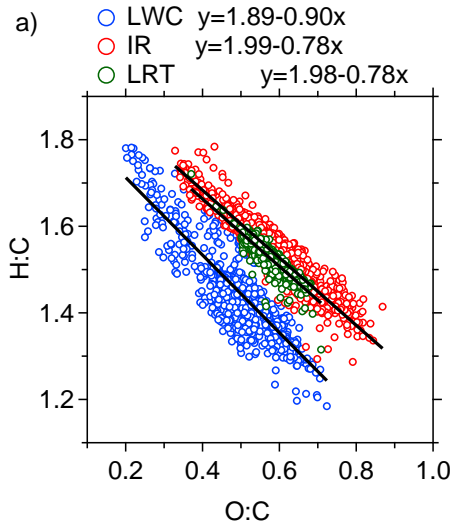
*Figure 3 a) Van Krevelen diagram for the three types of episodes; b) diurnal variation of carbon oxidation state*
*($\overline{OS}_c$ ). Means appear as circles with superimposed standard deviations.*

Legend: ■ Org small mode  ■ SO4 small mode  ■ Org large mode  ■ SO4 large mode

a-1 LWC
Mass-mode diameter (nm)
Small mode    211 ± 8
Large mode    539 ± 10

b-1 LWC
Mass-mode diameter (nm)
Small mode    197 ± 10
Large mode    585 ± 6

a-2 IR
Mass-mode diameter (nm)
Small mode    198 ± 9
Large mode    539 ± 8

b-2 IR
Mass-mode diameter (nm)
Small mode    204 ± 12
Large mode    605 ± 5

a-3 LRT
Mass-mode diameter (nm)
Small mode    200 ± 10
Large mode    532 ± 7

b-3 LRT
Mass-mode diameter (nm)
Small mode    196 ± 10
Large mode    571 ± 5

y-axis: $dM/dLogD_{va}$ (ug m$^{-3}$)
x-axis: $D_{va}$ (nm)

*Figure 4 Bimodal log-normal fitting results of the size distributions of organics and sulfate during the three types of episodes. a) Fitted small particle size mode and large particle size mode of organics during LWC, IR and LRT episodes; b) fitted small particle size mode and large particle size mode of sulfate during LWC, IR and LRT episodes.*
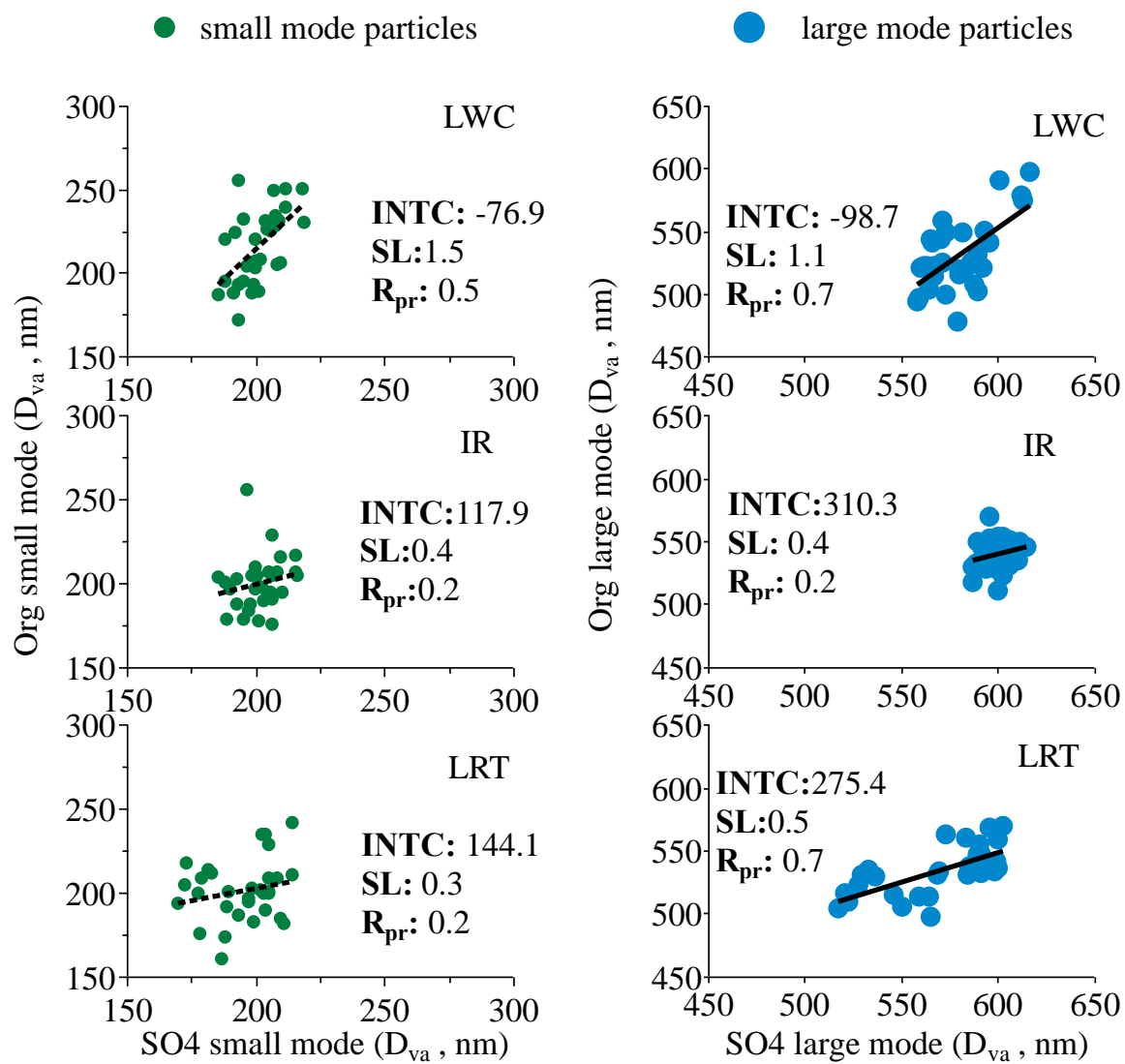
15
16  *Figure 5  Scatter plots and linear least square fits of mass-mode diameters of organics and sulfate during the three*
17  *different types of episodes. a1-a2) small and large mass-mode diameter of organics against sulfate during LWC*
18  *episodes; b1-b2) small and large mass-mode diameter of organics against sulfate during IR episodes; c1-c2) small*
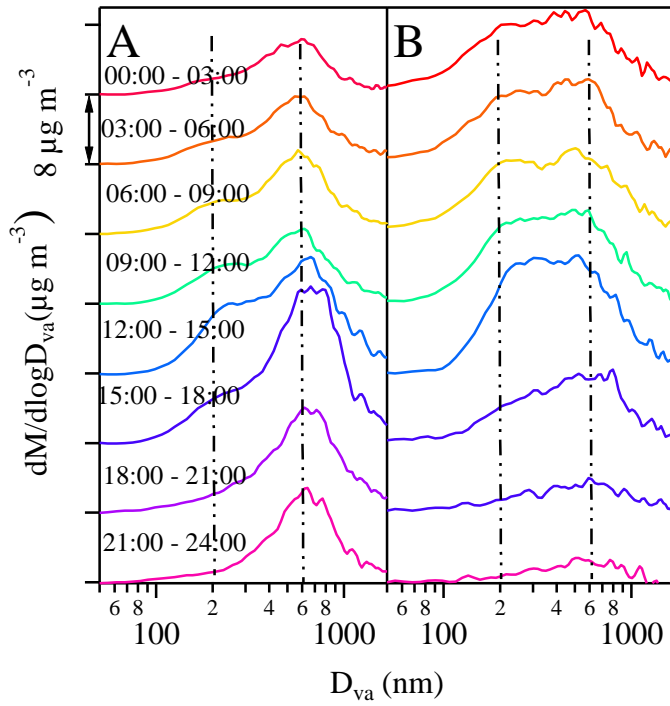19  *and large mass-mode diameter of organics against sulfate during LRT episodes.*
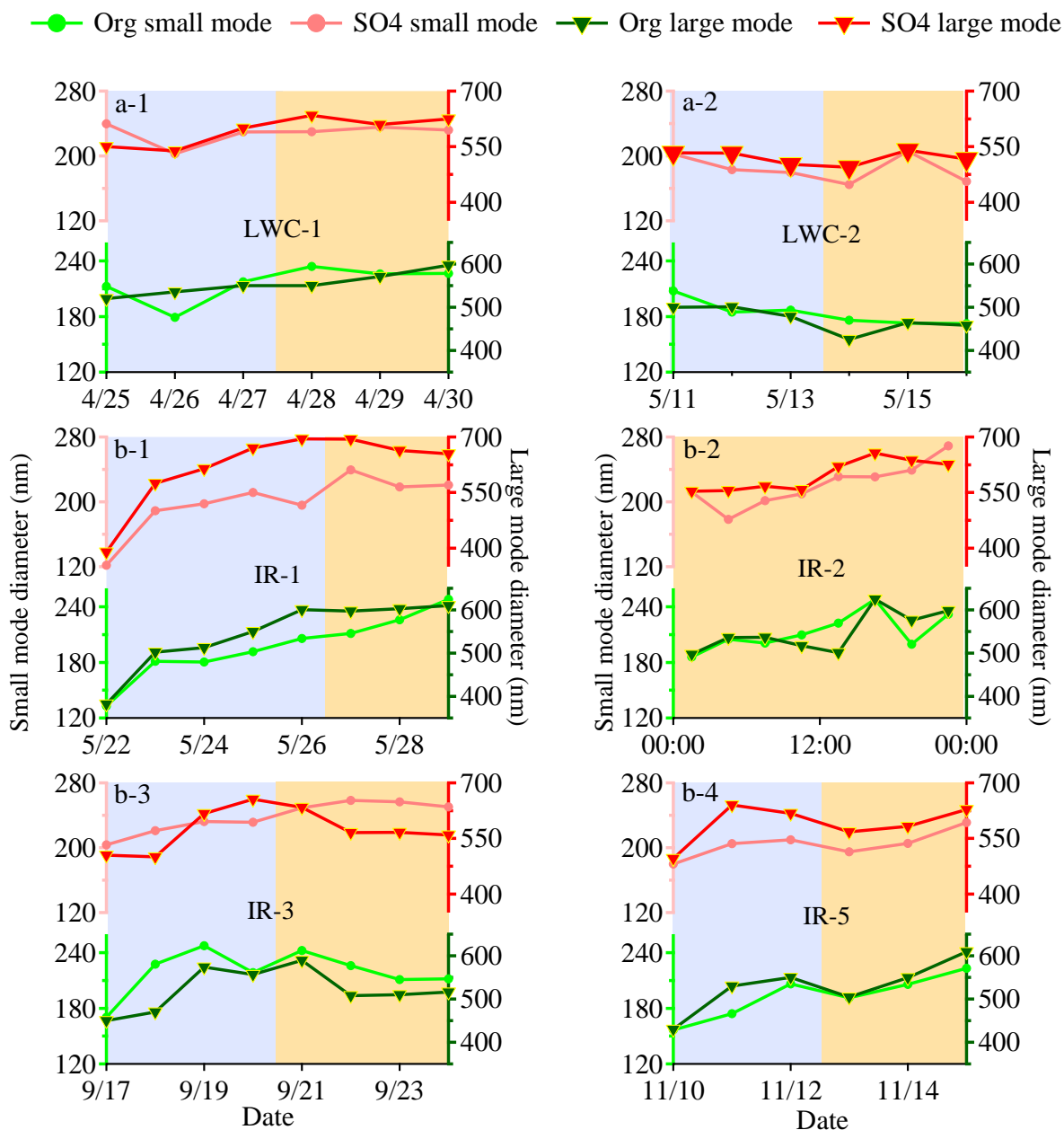
Figure 6 Variations of 24-hour averaged size distributions of fitted mass-mode diameters of organics and sulfates during LWC episodes and IR episodes (shaded in orange) and several days before each episode (shaded in blue). For the episode that lasted only for a day (E4), 3-hour averaged size distributions of fitted mass-mode diameters are shown instead. a) LWC episodes; b) IR episodes.

25
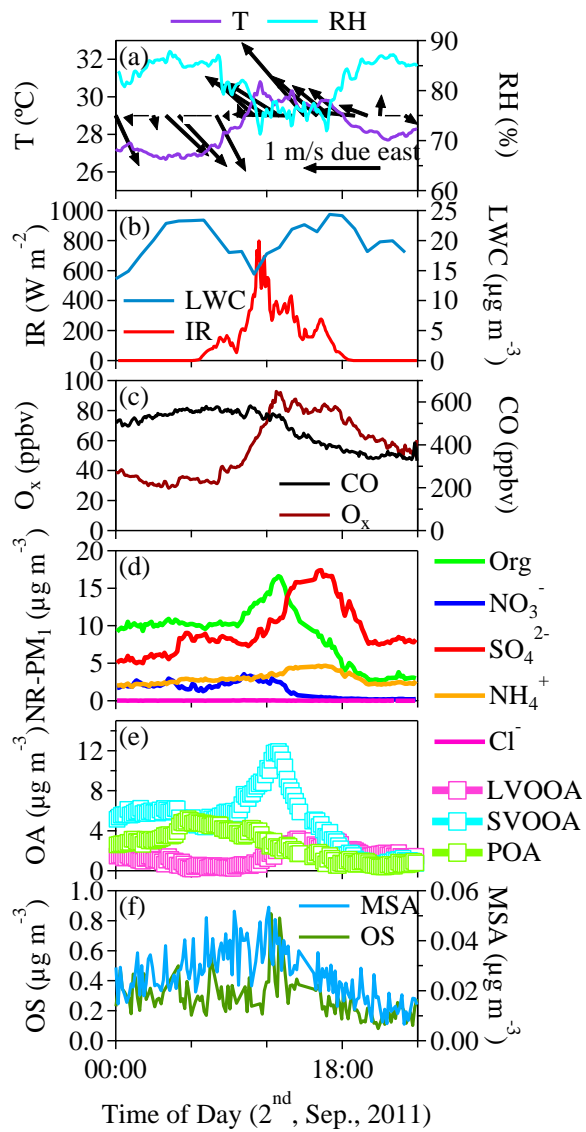
*Figure 7 Time series of meteorological parameters, gaseous species, NR-PM1 species and PMF-resolved organic*
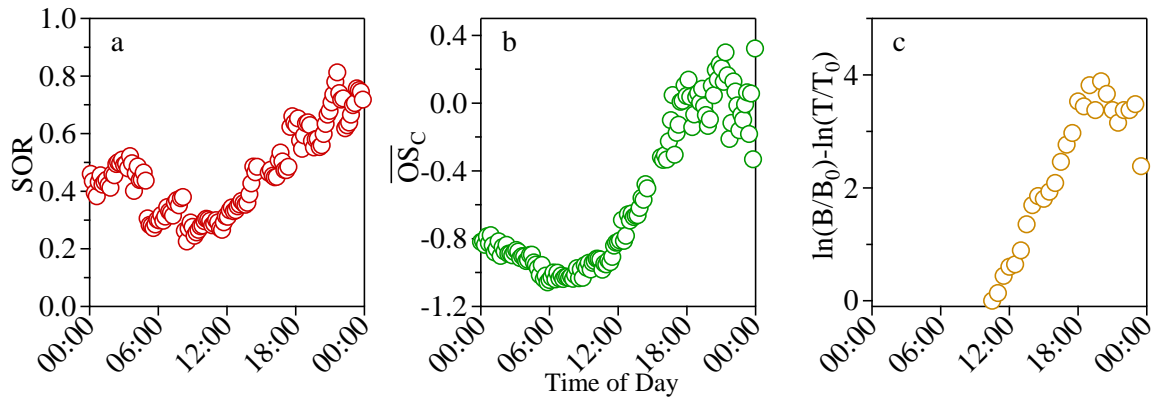*factors in E4.*

Sulfate    Organics

A
00:00 - 03:00
03:00 - 06:00
06:00 - 09:00
09:00 - 12:00
12:00 - 15:00
15:00 - 18:00
18:00 - 21:00
21:00 - 24:00

B

$8 \mu g \ m^{-3}$

$dM/dlogD_{va}(\mu g \ m^{-3})$

$D_{va}$ (nm)

28

29    *Figure 8 Size distributions of sulfate (A) and organics (B) in different time intervals during E4.*

30

30



31 *Figure 9 Oxidative evolution of aerosol components. a) Sulfur oxidation ratio (SOR); b) average carbon oxidation*
32 *state $\overline{OS_c}$; c) benzene to toluene ratio (B: benzene concentration at time t; B0: benzene concentration at time 0; T:*
33 *toluene concentration at time t; T0: toluene concentration at time 0).*

34
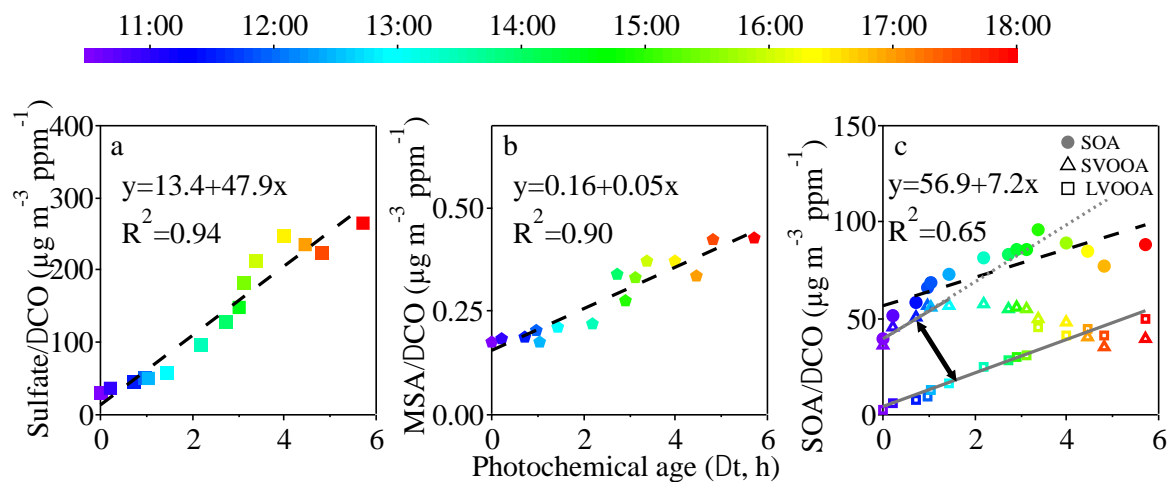
*Figure 10 Photochemical production of secondary species. a)$\Delta$CO-normalized sulfate concentration (SO4/$\Delta$CO) as a function of photochemical age; b)$\Delta$CO-normalized MSA concentration (MSA/$\Delta$CO) as a function of photochemical age; and c)$\Delta$CO-normalized secondary organic aerosol concentration (SOA/$\Delta$CO, SOA(SVOOA+LVOOA)) as a function of photochemical age. Data points are colored by time of day. Data points represent half-hour averages.*

40
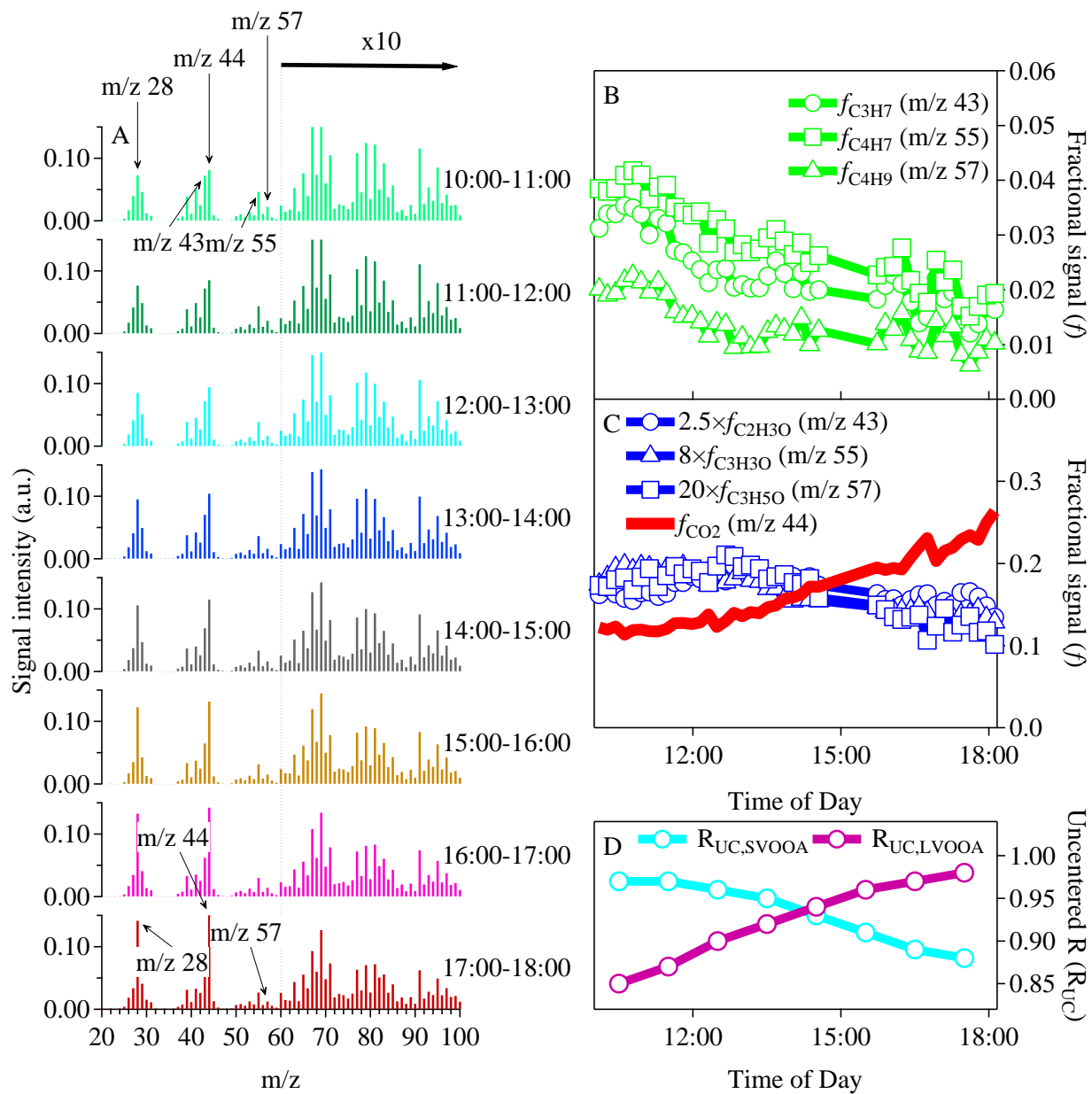
*Figure 11 Evolution of high-resolution organic mass spectra from 10:00 to18:00 during the photochemical aging*
*process in E4: a) mass spectral evolution; b) changes in relative intensities of hydrocarbon-like ions $C_3H_7^+$ (m/z 43),*
*$C_4H_7^+$(m/z 55) and $C_4H_9^+$(m/z 57); c) changes in relative intensities of oxygen-containing ions: $C_2H_3O^+$(m/z 43),*
*$C_3H_3O^+$(m/z 55), $C_3H_5O^+$(m/z 57) and $CO_2^+$(m/z 44); and c) correlation of OA mass spectra with reference* (Mohr et
al., 2012) *SVOOA and LVOOA mass spectra.*